The ARMM System: An Optimized Mobile Electromagnetic Coil for Non-Linear Actuation of Flexible Surgical Instruments

Jakub Sikorski[1], Christoff M. Heunis[1], Federico Franco[1], and Sarthak Misra[1,2]

[1]Department of Biomechanical Engineering, University of Twente, 7500 AE Enschede, The Netherlands
[2]Department of Biomedical Engineering, University of Groningen and University Medical Centre Groningen, 9713 GZ Groningen, The Netherlands

Automation of flexible surgical instruments requires the development of robotic technologies capable of small-scale power transmission. Magnetic actuation has successfully been used for that purpose. Nevertheless, current systems for magnetic actuation suffer from small workspaces or poor bandwidth of magnetic field control. In this work, we design, develop, and test a novel magnetic actuation system called Advanced Robotics for Magnetic Manipulation (ARMM). The ARMM system employs a 6 DoF mobile electromagnetic coil capable of generating prescribed magnetic fields and gradients. The mobile coil approach allows for easy scaling of the actuation workspace, which depends on the range of robotic arm, and in our case spans up to 1.3 m. Due to limited end-effector payload of the robotic arm used in the ARMM system, the mobile coil has been designed using an optimization routine. For a given mass and heat dissipation constraints, this routine provides the coil geometry that maximizes the average magnetic field generated in the target region. Since the Vacoflux core of the fabricated coil saturates within operational conditions, we propose an actuation strategy employing an online-updated iterative map technique. Using this map, the ARMM system allows for precise generation of prescribed magnetic fields and gradients at the point of interest, while taking into account the effects of the non-linearities due to core saturation. The strategy is validated experimentally, showing the average error of 2.34% for magnetic field and 7.20% for the magnetic field gradient.

Index Terms—**Magnetic devices, magnetic variables control, medical robotics.**

I. Introduction

STEERING and positioning of flexible surgical instruments, such as medical catheters in blood vessels during endovascular interventions is a challenging task, which may involve high-risk complications [1]. Although accessing most target areas within the human cardiovascular system is usually technically feasible, safe manual navigation of catheters inside these areas is highly dependent on the abilities of clinicians involved, requiring them to undergo expensive and time-consuming training [2]. Automating the guidance of catheters using the principles of surgical robotics can in the future mitigate those problems, vastly expanding the range of minimally invasive procedures, which can be safely realized using such catheters.

Nevertheless, integrating surgical robotic technologies in endovascular catheters still requires the development of new actuation techniques, capable of transmitting power at small scales [3]. A range of promising catheter designs employs magnetic actuation for that purpose [4]. These catheters are fit with ferromagnetic elements that, if subjected to an external magnetic field, experience magnetic wrenches due to the Lorentz force. These wrenches comprise of both torque and force. The magnetic torque is dependent directly on the external magnetic field, whereas the magnetic force is determined by the spatial gradient of the field in the location of the magnetic element. These wrenches can be used for non-contact steering of a catheter inside the body of a patient, provided a system capable of controlling the field and its gradient in adequate volume [5], [6].

Two principal classes of systems for magnetic actuation are presented in the literature. The first class involves those systems, which employ multiple electromagnetic coils organized into an array around a target volume [5]–[7]. These systems offer strong magnetic fields, although they exhibit poor workspace scalability, whereby increasing the target volume negatively affects the maximum control bandwidth of the system. Alternatively, several studies propose using mobile permanent magnets [8]–[12]. Those systems are capable of operating in larger workspaces. Nevertheless, as the strength of the field provided by permanent magnets cannot be changed, they require complicated actuator design and advanced motion planning algorithms for successful operation. Furthermore, the presence of non-decaying sources of the magnetic field poses danger to personnel in the vicinity of the system, requiring safety protocol comparable to that of magnetic resonance systems.

The first notion that the advantages of both classes of magnetic actuation systems can be combined by using mobile electromagnetic coils was proposed by Veron *et al.* [13], suggesting that mobile serial-link robotic actuators may prove to offer clinically relevant workspaces, while decreasing labor costs, and improving ergonomics and workspace accessibility for the surgeons performing magnetically guided procedures. Several studies further explore the idea of using mobile coils for actuation of various medical instruments; however, none of them presents a formalized design and implementation of such system [14]–[16].

Manuscript received August 22, 2018; revised November 30, 2018 and February 1, 2019; accepted March 28, 2019. *(Jakub Sikorski and Christoff M. Heunis contributed equally to this work)* Corresponding author: J. Sikorski (e-mail: j.sikorski@utwente.nl).

Color versions of one or more of the figures in this paper are available online at http://ieeexplore.ieee.org.

Digital Object Identifier 10.1109/TMAG.2019.2917370

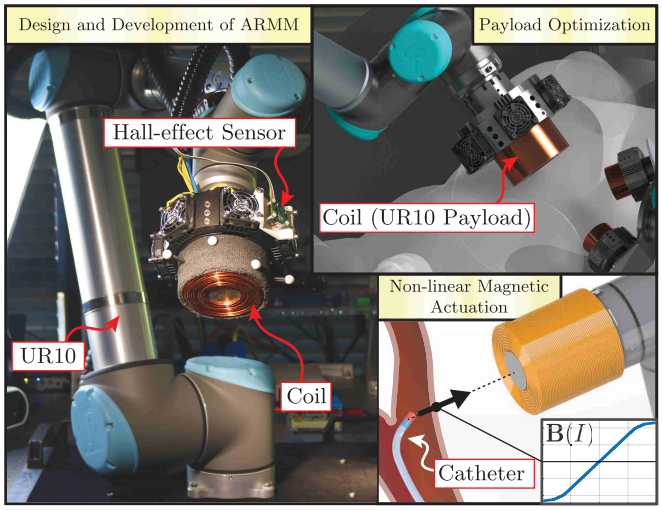

Fig. 1. Magnetic actuation systems can be used for non-contact actuation of flexible catheters. In this paper, we present the design and development process of the ARMM system. The ARMM system comprises 6 DoF mobile electromagnet and is capable of providing magnetic actuation within a spherical workspace with a radius of 1300 mm. Due to the limited payload of the UR10 robotic arm (Universal Robots, Odense, Denmark) employed in the ARMM system, we propose an optimization strategy to design the electromagnet generating the largest magnetic field possible under a heat dissipation constraint. Furthermore, we propose a strategy to generate a prescribed magnetic field ($\mathbf{B}(I)$) and its spatial gradient using the ARMM system. The strategy employs an online-updated iterative map, which uses a Hall effect sensor to account for the non-linearities of the field due to coil saturation at high currents.

Drawing inspiration from these ideas, in this paper, we propose a novel system for magnetic actuation. The Advanced Robot for Magnetic Manipulation (ARMM) system (Fig. 1) employs a single, cored electromagnetic coil attached to a 6 DoF robotic arm. Due to coil mobility, it offers the benefit of a much larger workspace than the one provided by devices employing stationary electromagnets. Moreover, it alleviates challenges induced by systems employing permanent magnets as it provides a greater range of controllable magnetic fields, including the capability to be switched off when necessary.

We begin this paper by presenting a detailed design of the ARMM system in the context of a clinically relevant catheter steering framework. We put particular emphasis on the design of the electromagnetic coil. As the limited payload of the robotic arm constrains the total size of the electromagnet, we propose an optimization routine that determines the composition of the coil resulting in the maximum magnetic field generated for a given mass constraint. The routine takes into account the fact that the cross section of the windings of the coil must result in coil resistance resulting in heat dissipation below a tolerable limit. Using the optimization as a design tool has recently been proposed for linear, coreless electromagnets [17]. To the best of our knowledge, this work is the first study aimed at designing a payload-optimal electromagnet with ferromagnetic core for magnetic actuation inside a clinically relevant workspace.

The presence of a ferromagnetic core significantly increases the field generated by the mobile coil. Nevertheless, it complicates the modeling of the coil at higher currents, as the resulting field-to-current relation becomes non-linear once the core reaches its saturation limit [18]. The use of Hall effect sensors for on-line correction of the coil model has been proposed to overcome this problem [19], [20]. However, the approach presented therein neglects the fact that the superimposed magnetic fields of the core and the windings have different spatial distributions. This leads to a systematic correction error. In this work, we propose an alternative, exact approach for integrating Hall-effect sensors for on-line control of the electromagnetic coil. Thus, we can use the ARMM system for precise magnetic actuation past the saturation region.

Finally, we present an actuation strategy in which the ARMM system is used to generate codirectional, prescribed magnetic fields and forces with independently controlled magnitudes. We test the strategy in a series of experiments, whereby we control and measure the magnitudes of both the magnetic field and its spatial gradient. The latter quantity has been validated using a method previously applied in micro-electromechanical systems, in which the spatial gradient is measured indirectly, using magnetically compatible force sensor [21].

II. Design of the ARMM System

In this section, we present the composition of the ARMM system, which resulted from a cyclic process of material prototyping, testing, and iterative analysis. This section introduces the system integration of the ARMM system, including the catheter insertion device and the tracking capabilities of the system. Particular emphasis is put on the electromagnet design, which results from an optimization routine taking into account the limitations of the serial manipulator used in the system. The design parameters for the electromagnetic coil are determined by maximizing the average magnetic field in the operational region, while constraining the possible solutions, taking the tolerable coil temperature rise and payload limitations into account.

A. System Composition and Magnetic Manipulation Strategy

We begin the development process by analyzing the principles of magnetic actuation in the context of catheters. This allows us to identify a set of requirements, which have to be fulfilled by a successful system for magnetic actuation. Magnetic actuation is used to exert a wrench ($\mathbf{W} \in \mathbb{R}^3$) on a permanent dipole attached to a catheter. This dipole is located at a point ($\mathbf{p} \in \mathbb{R}^3$) and is represented by a magnetic dipole moment ($\boldsymbol{\mu} \in \mathbb{R}^3$). The magnetic wrench relates to the external magnetic field ($\mathbf{B}(\mathbf{p}) \in \mathbb{R}^3$) and its spatial gradient as follows:

$$\mathbf{W} = \begin{bmatrix} \mathbf{F}_\mu \\ \boldsymbol{\tau}_\mu \end{bmatrix} = \begin{bmatrix} \nabla(\boldsymbol{\mu}^T \mathbf{B}(\mathbf{p})) \\ S(\boldsymbol{\mu})\mathbf{B}(\mathbf{p}) \end{bmatrix} \tag{1}$$

where $S(\boldsymbol{\mu})$ denotes a skew-symmetric form of $\boldsymbol{\mu}$.

We identify three principal design requirements for a successful magnetic actuation system. First, it should be capable of deflecting a catheter in any direction by using magnetic wrench ($\mathbf{W}$). Furthermore, the magnitudes of torque and force components of $\mathbf{W}$ should be controllable, and as large as possible. Finally, a catheter used during an endovascular

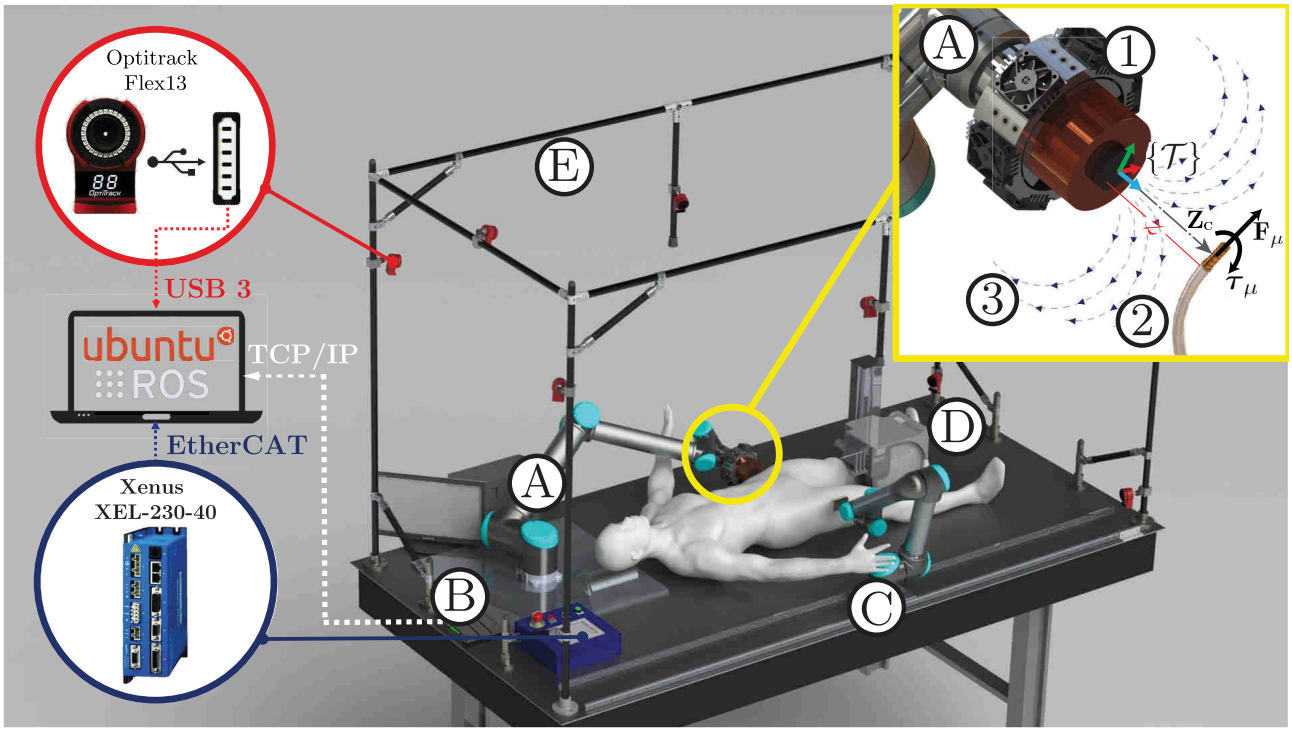

Fig. 2. Ⓐ ARMM system is a magnetic actuation system that is designed to guide flexible surgical instruments, such as endovascular catheters, in a clinically relevant workspace. The framework supporting the operation of the ARMM system includes Ⓑ digital control network, Ⓒ assistive robotic arm UR5 (Universal Robots, Odense, Denmark)—in this study, it is used for sensor positioning—and Ⓓ catheter insertion device. The workspace is surrounded by Ⓔ truss structure, containing eight Optitrack Flex 13 (NaturalPoint, Inc., Corvallis, USA) cameras used for registering and tracking objects inside the workspace. The magnetic actuation strategy employed in the ARMM system uses ① mobile coil to steer ② endovascular catheter by generating ③ magnetic field. When exposed to this field, a catheter equipped with a magnetic dipole experiences magnetic force ($\mathbf{F}_\mu \in \mathbb{R}^3$) and torque ($\boldsymbol{\tau}_\mu \in \mathbb{R}^3$). UR10 is used to align the coil axis of symmetry ($\mathbf{Z}_C \in \mathbb{R}^3 : \|\mathbf{Z}_C\| = 1$) with the center of the catheter tip. Such configuration allows to control the values of $\mathbf{F}_\mu$ and $\boldsymbol{\tau}_\mu$ by varying the current ($I \in \mathbb{R}$) in the coil and the distance ($z \in \mathbb{R}^+$) from the dipole to the face of the coil, as measured in coil local reference frame ($\mathcal{T}$).

intervention needs to be navigated over large distances. Thus, the successful magnetic-actuation system should provide precise steering capabilities at every point along the required trajectory, regardless of the pose of the catheter inside the body.

The ARMM system, proposed in this paper, is presented in Fig. 2. It implements a 6 DoF mobile coil approach, which allows generating magnetic fields and gradients in any direction in a scalable workspace, the size of which depends on the reach of the robotic arm used [13]. We use the UR10 (Universal Robots, Odense, Denmark), which has a spherical workspace with a radius of 1300 mm and can carry loads up to 10 kg with a 0.1 mm repeatability. Since it is a collaborative robot, its design ensures safety in clinical environments. The robot is located on the operative table alongside a UR5 (Universal Robots, Odense, Denmark) serial arm, used to position sensors or medical imaging devices, such as ultrasound transducers.

The steering strategy employed for the actuation of a catheter using the ARMM system assumes knowledge of the point ($\mathbf{p}$), at which the dipole ($\boldsymbol{\mu}$) attached to the catheter is located. We fit a local reference frame ($\{\mathcal{T}\}$) onto the front face of the coil, such that the coil symmetry axis ($\mathbf{Z}_C \in \mathbb{R}^3 : \|\mathbf{Z}_C\| = 1$) is coincident with the Z axis of $\{\mathcal{T}\}$. Subsequently, we assume that the UR10 robot is capable of positioning the coil, such that $\mathbf{p}$ is coincident with $\mathbf{Z}_C$ at all times (Fig. 2). Thus, the magnetic field at $\mathbf{p}$ can be expressed as follows:

$$\mathbf{B}(\mathbf{p}, I) = \mathbf{Z}_C B(z, I) \tag{2}$$

where $z \in \mathbb{R}^+$ is the distance of the dipole ($\boldsymbol{\mu}$) from the face of the coil along the axis ($\mathbf{Z}_C$) and $B(z, I) : \mathbb{R}^+ \times \mathbb{R} \mapsto \mathbb{R}$ is the scalar value of the magnetic field along the axis ($\mathbf{Z}_C$). If the rotational matrix ($\mathbf{R}_\mathcal{T} \in \mathrm{SO}(3)$) describes the orientation of coil frame ($\{\mathcal{T}\}$), (1) can be reduced to

$$\begin{bmatrix} \mathbf{F}_\mu \\ \boldsymbol{\tau}_\mu \end{bmatrix} = \begin{bmatrix} \mathbf{0}_{3\times1} & \mathbf{R}_\mathcal{T} \nabla \mathbf{B}_0 \mathbf{R}_\mathcal{T}^T \boldsymbol{\mu} \\ S(\boldsymbol{\mu})\mathbf{Z}_C & \mathbf{0}_{3\times1} \end{bmatrix} \underbrace{\begin{bmatrix} B(z, I) & \dfrac{\partial B}{\partial z} \end{bmatrix}^T}_{\mathbf{b}} \tag{3}$$

$$\nabla \mathbf{B}_0 = \mathrm{diag}(\begin{bmatrix} -0.5 & -0.5 & 1 \end{bmatrix}). \tag{4}$$

This choice of actuation technique is motivated by previous studies involving steering of magnetic catheters. The magnetic torques have been shown to have a higher impact on the deflection than magnetic forces, and hence, the effect of the latter is often neglected [6], [19], [22]. In the same time, our technique ensures the presence of a force coincident with the torque bending plane, improving the stability of the catheter at larger deflections [23]. Furthermore, the UR10 robot can reposition itself with speeds of up to 1 m/s, which is sufficient to follow catheters that move significantly slower [24].

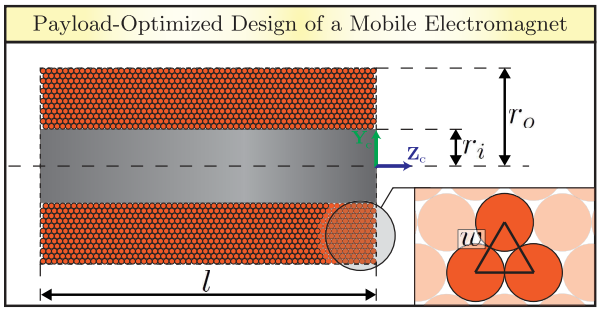

Fig. 3. Model of coil geometry used in the optimization routine presented in this paper. The coil comprises two individual parts: a cylindrical core and n windings of copper wire with diameter ($w \in \mathbb{R}^+$). The length ($l \in \mathbb{R}^+$) of both the core and the windings is the same. The core occupies the inner portion of the coil, up to the distance ($r_i \in \mathbb{R}^+$), whereas the windings are arranged around it into layers reaching up to the final radius of the core ($r_o \in \mathbb{R}^+$). The proposed optimization routine finds the combination of parameters (w, r_i, r_o, l) resulting in the highest magnetic field in the desired workspace while taking into account the temperature and payload constraints.

In previous studies, the torque ($\boldsymbol{\tau}_\mu \in \mathbb{R}^3$) has been identified as the primary component of $\mathbf{W}$ used to deflect flexible magnetic catheters. As follows from (3), both the magnitude and the direction of this torque are proportional to the magnitude of the magnetic field ($B(z, I)$). Thus, designing an end-effector electromagnetic coil for the ARMM system should aim at maximizing the magnetic fields generated by it at a certain distance (z) from its face. As the coil is positioned outside the human body, we assume that the catheter at any instance during the procedure is located between 5 and 20 cm away from the coil. Thus, our aim is to design a coil that maximizes the field generation within that region.

B. Payload-Optimized Design of a Mobile Electromagnet

In contrast to other systems, where stationary coils can be made as large as possible to generate fields within the desired specifications, the UR10 robotic arm used in the ARMM system can carry a maximum payload ($m_m = 10$ kg), which limits the maximum size of the coil. This problem can be overcome by driving the coil with a larger maximum current ($I = I_m$), although this can lead to excessive coil heat dissipation. Thus, we employ an optimization routine, allowing us to determine the optimal design of the coil, maximizing actuation capabilities of the coil under payload and heat dissipation constraints.

We limit our investigation to ferrous-core solenoid coils, due to their reliability and ease of manufacturing. The geometry of such a coil (Fig. 3) can be described by a cylinder with length ($l \in \mathbb{R}$). The inner portion of the cylinder is occupied by the ferromagnetic core with average density ($\rho_c \in \mathbb{R}^+$) and radius ($r_i \in \mathbb{R}^+$). The rest of the coil the coil comprises of ($n \in \mathbb{R}^+$) turns of copper wire, with average density ($\rho_w \in\in \mathbb{R}^+$), electrical resistivity ($\alpha \in \mathbb{R}^+$), and diameter ($w \in \mathbb{R}^+$). The turns are organized in as many layers as possible, not exceeding the outer radius of the outer radius of the coil ($r_o \in \mathbb{R}^+$). The maximum number of turns of the wire (n), which can be assembled into a coil with certain geometry depends on the filling factor. For the best case scenario (Fig. 3), n is given by given by

$$n = \left\lfloor \frac{l(h-2w)\sqrt{3}}{6w^2} + \frac{l}{2w} - \frac{(h-2w)\sqrt{3}}{6w} - \frac{1}{2} \right\rfloor \tag{5}$$

where ($h = r_o - r_i$), and $\lfloor\,\rfloor$ is the flooring operator.

The two variables used to constrain the proposed optimization are the mass ($m \in \mathbb{R}^+$) thermal power ($P \in \mathbb{R}^+$) of the solenoid. They can be calculated as follows:

$$m = \pi l\left(\rho_w\left(r_o^2 - r_i^2\right) + \rho_c r_i^2\right) \tag{6}$$

$$P = I_m^2 \alpha \frac{nh}{w^2}. \tag{7}$$

Relation (6) determines directly the set of possible coil geometry parameters constraining the mass of the coil below the payload limit. Thus, (6) is used as a constraint in the used as a constraint in the optimization scheme. On the other hand, determining the maximum acceptable thermal power of the coil is challenging, due to the complexity of models describing heat dissipation within the material. Thus, in order to convert (7) into a practical constraint, we decide to consider a worst case heating scenario. We assume that the coil is a closed thermal system, i.e., no heat is exchanged with

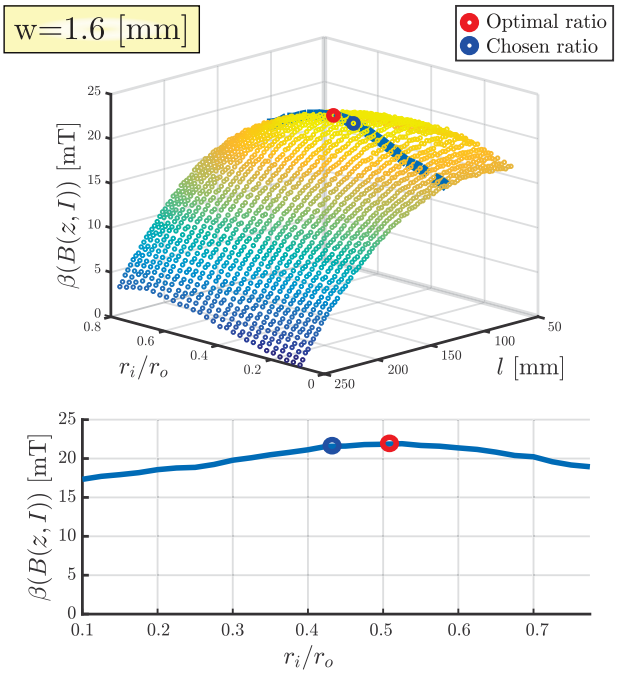

Fig. 4. Optimization routine (10) is employed in the design of the electromagnetic coil for the ARMM system. Since the full 4-D optimization space is impossible to visualize, we reduce the number of variables to highlight the main findings of the procedure. Selection of results for the final wire diameter ($w = 1.6$ mm) (top). The results are generated for a selection of coil lengths (l) and ratios of the and outer radii of the coil (r_i/r_o). The value of the radii are computed using (6) such that the mass of the coil is as large as possible for each ratio. Cross section of the results for the optimized length ($l = 110$ mm) resulting in highest average value of average value of the field $\beta(B(z, I))$ (bottom). The optimal r_i/r_o is 0.527, resulting in the inner radius. However, seeing the neighborhood of the final solution, we notice that the dependence of the solution on the ratio r_i/r_o is not significant. Thus, without losing much performance, we select a smaller ratio of 0.425, which results in the inner diameter of $r_i = 45$ mm, corresponding to the size of the coiling tool available to our manufacturer.

TABLE I
SPECIFICATIONS OF THE ARMM SYSTEM ELECTROMAGNETIC COIL

Specification / characteristic	Value / description
Copper-wire electromagnetic coil (Wijdeven, Oirschot, Netherlands)	
Outer diameter ($2\,r_o$) [mm]	105
Inner diameter ($2\,r_i$) [mm]	45
Length (l) [mm]	110
Wire diameter (w) [mm]	1.6
Turns (n)	1282
DC Resistance [Ω]	2.6
Specific heat (c_w, c_c - assumed equal) $\left[\frac{J}{kg*K}\right]$	400
Density (ρ_w) $\left[\frac{kg}{m^3}\right]$	8500
Resistivity (α) $\left[\frac{\Omega}{m}\right]$	$1.7 * 10^{-8}$
Vacoflux 50 core (Sekels, Ober-Mörlen, Germany)	
Length [mm]	135
Density (ρ_w) $\left[\frac{kg}{m^3}\right]$	8120
Treatment	Magnetic annealing; Corrosion protection
Saturation magnetization [T]	2.35

the relate the thermal power to a predicted temperature rate ($\dot{T} \in \mathbb{R}$) of the coil running continuously at I_m as follows:

$$\dot{T} = PC_a \tag{8}$$

where ($C_a \in \mathbb{R}^+$) is the heat capacity of the coil approximated by the following relation:

$$C_a = \pi l\left(c_w \rho_w \left(r_o^2 - r_i^2\right) + c_c \rho_c r_i^2\right) \tag{9}$$

using the specific heats of wire ($c_w \in \mathbb{R}^+$) and of the core ($c_c \in \mathbb{R}^+\mathbb{R}^+$), respectively. Note that we disregard the dependence of wire resistivity temperature. It can be ignored as long as the total temperature increase of the coil is kept within 25 °C–40 °C (resistivity increase of 10%–15%) [25].

Subsequently, the optimal geometry of the coil can be calculated by solving the following maximization problem:

$$\max_{r_o, r_i, l, w \in \mathbb{R}^+} \quad \beta(B(z, I)) \tag{10}$$

$$\text{s.t.} \quad m \leq m_m, \ \dot{T} \leq \dot{T}_m, \ r_i < r_o \tag{11}$$

where the function ($\beta(B(z, I)) : \mathbb{R}^+ \times \mathbb{R} \mapsto \mathbb{R}^+\mathbb{R}^+$) provides information about the optimality of the particular field distribution depends on the design requirements. In case of the coil designed for the ARMM system, we maximize the average maximize the average field generated along the long axis ($\mathbf{Z}_C$) of the coil, between 5 and 20 cm away from the face of the coil. Thus, the proposed $\beta(B(z, I))$ is as follows:

$$\beta(B(z, I)) = \frac{1}{0.15} \int_{0.05}^{0.2} B(z, I_m) dx. \tag{12}$$

Since $B(z, I)$ for a given coil geometry is challenging to establish analytically, it is usually approximated using simplified models [26] or finite element (FE) simulations [6].

C. Final Coil Design

The optimization problem (10) is solved by taking into account the constraints established in the process of designing the ARMM system. The maximum mass (m_m) was set to 8 kg

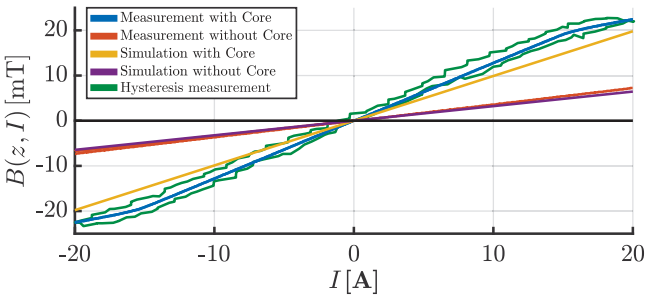

Fig. 5. Senis 3MH3A-500MT (Senis AG, Baar, Switzerland) teslameter is used to measure the value of the magnetic field ($B(z, I)$) generated by the coil of the ARMM system at the location ($z = 10$ cm) in the entire operational range of current (I). The results are compared to predictions from the FE model used in the design process. The measurements and simulations are performed for the coil with and without the Vacoflux core. The graph shows that the coil produces more magnetic field than predicted by the model. This is mostly due to the better magnetic properties of the core. Furthermore, an additional fast sweep (green) across the entire operational current range in 0.5 s. This was performed to investigate the presence of hysteretic behavior during sudden current variations, as motivated by our previous experience with similar electromagnets. Limited hysteretic behavior is observed. However, since such sudden variations in current are unlikely to occur during catheter steering tasks, we neglect this behavior. Nevertheless, the coil exhibits saturation in the operational range. As this phenomenon makes the actuation non-linear for any rate of current, it needs to be taken into account while using ARMM for precise magnetic actuation.

to leave enough payload for fasteners and sensors. The maximum tolerable initial temperature rate ($\dot{T}_m$) is set arbitrarily at (0.1 K/s). A parametric model of the coil is developed using COMSOL 5.2 (COMSOL, Burlington, VT, USA) FE solver and linked with MATLAB 2017b (MathWorks, Natick, MA, USA) routine using LiveLink utility. By solving the model, we obtain the field distribution for a given set of parameters (r_o, r_i, l, w). The average computation time for a solution corresponding to a particular geometry is 2.7 s. Results of the optimization are presented in Fig. 4, whereas the parameters of the coil manufactured using the geometry calculated by our optimization scheme are provided in Table I.

The prototype of the coil is assembled and characterized by using a teslameter to measure the magnetic field ($B(z, I)$) at a distance ($z = 10$ cm) generated at a full, operational range of currents (I). Subsequently, the same procedure is performed without the Vacoflux core. The results (Fig. 5) are compared to the outcome of the COMSOL model used during the design. We observe that the total field generated by the coil is larger than the model predictions. This is mostly due to the magnetization of the Vacoflux core, as the difference between the experimental data and the model for the magnetic field of the coil windings without the core is negligible. The field generated by the core exhibits non-linearities due to saturation in its operational region (on the contrary to predictions from the model). In the remainder of this paper, we propose a novel magnetic actuation strategy, which takes this phenomenon into account.

III. NON-LINEAR MAGNETIC ACTUATION USING THE ARMM SYSTEM

In this section, we propose a non-linear, iterative technique, for the precise, real-time generation of prescribed magnetic

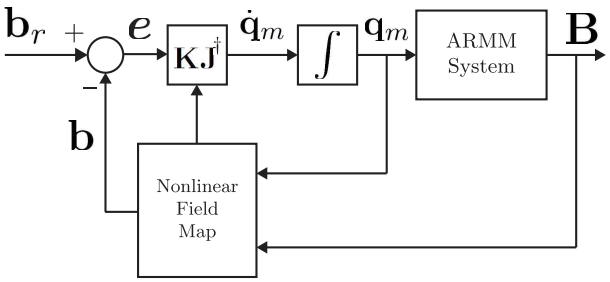

Fig. 6. ARMM system employs an iterative field map to generate reference magnetic field and its gradient $\mathbf{b}_r = \left[B_r \ (\partial B_r/\partial z)\right]^T$ at $\mathbf{p}$. The information about the configuration ($\mathbf{q}_m = \left[z \ I\right]^T$) of the system, as well as measurements from magnetic field sensor are used to generate an error signal ($\mathbf{e} \in R^2$). The error is minimized using a Jacobian inverse scheme, employing the derivation presented in (15). † denotes damped pseudo-inverse, used in place of regular matrix inverse for improved stability [27]. The gain ($\mathbf{K} \in \mathbb{R}^{2\times2} : \mathbf{K} > 0$) of the scheme is tuned manually until satisfactory performance is achieved.

fields and gradients using the ARMM system. This technique employs an online-updated inverse map of ARMM to compute the configuration of the system generating reference magnetic fields and gradients. Our approach can be used to generate mutually orthogonal magnetic forces and torques with independently controlled magnitudes.

The task of the iterative map is to find the appropriate configuration of the ARMM system ($\mathbf{q}_m = \left[z \ I\right]^T$), corresponding to the reference magnetic variables ($\mathbf{b}$) as defined in (3). Since the coil used in the ARMM system exhibits saturation in its operational region, we separately model the magnetic field components generated by the windings and by the Vacoflux core. Hence, the total field ($B(z, I)$) can be modeled as a superposition of those two components as follows:

$$B(z, I) = I(B_w(z) + \eta(I)B_c(z)) \tag{13}$$

$$\frac{\partial B}{\partial z}(z, I) = I\left(\frac{\partial B_w}{\partial z} + \eta(I)\frac{\partial B_c}{\partial z}\right) \tag{14}$$

where $\eta(I) : \mathbb{R} \mapsto (0; 1]$ is the saturation model of the core, and $B_w, B_c \in \mathbb{R}^+$ are the unit field maps of the windings and the core at the distance (z).

Furthermore, we can relate the rates of change of $\mathbf{b}$ and $\mathbf{q}_m$ through a Jacobian matrix ($\mathbf{J} \in \mathbb{R}^{2\times2}$)

$$\dot{\mathbf{b}} = \mathbf{J}\dot{\mathbf{q}}_m = \begin{bmatrix} \frac{\partial B}{\partial z} & \frac{\partial B}{\partial I} \\ \frac{\partial^2 B}{\partial z^2} & \frac{\partial^2 B}{\partial I \partial z} \end{bmatrix} \dot{\mathbf{q}}_m. \tag{15}$$

Using the magnetic field model (13), (14), we derive the entries of the Jacobian as follows:

$$\frac{\partial^2 B}{\partial I \partial z} = \frac{\partial B_w}{\partial z} + \left(I\frac{d\eta}{dI} + \eta(I)\right)\frac{\partial B_c}{\partial z} \tag{16}$$

$$\frac{\partial^2 B}{\partial z^2} = I\left(\frac{\partial^2 B_w}{\partial z^2} + \eta(I)\frac{\partial^2 B_c}{\partial z^2}\right) \tag{17}$$

$$\frac{\partial B}{\partial I} = B_w(z) + \left(I\frac{d\eta}{dI} + \eta(I)\right)B_c. \tag{18}$$

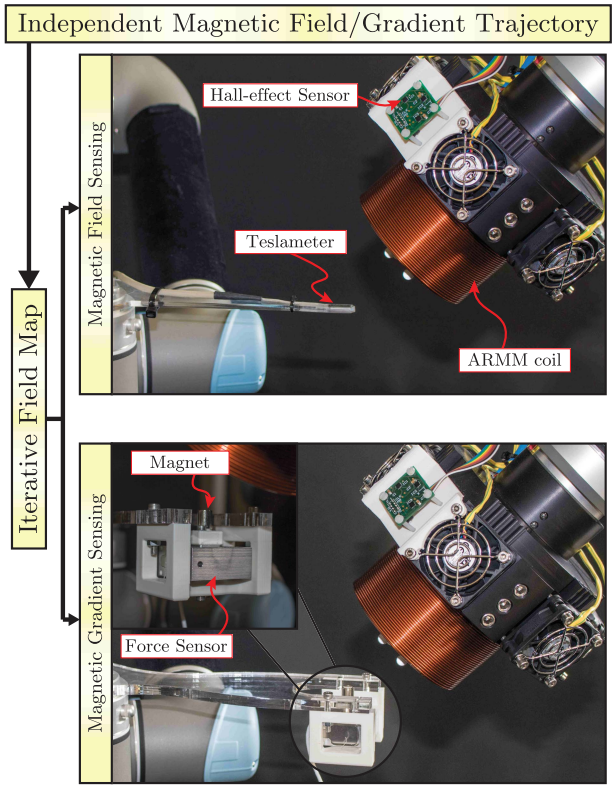

Fig. 7. Setup used to validate the iterative map proposed in Section III. In this experiment, the ARMM system is used to generate prescribed magnetic field/gradient trajectories for a selected point ($\mathbf{p} \in \mathbb{R}^3$). Initially, a Senis 3MH3A-500MT (Senis AG, Baar, Switzerland) teslameter is used to sense the magnetic field at $\mathbf{p}$ for the duration of the trajectory. Following that, the teslameter is replaced by a permanent dipole with known magnetic dipole moment ($\boldsymbol{\mu}$) attached to a K3D40 force sensor (Meβsysteme AG, Henningsdorf, Germany) and the trajectory is repeated. The measurements from the force sensor are processed to recreate the magnetic field gradient generated by ARMM. Both sensors are precisely positioned at $\mathbf{p}$ using the UR5 robotic arm (Universal Robots, Odense, Denmark) to ensure that the measurements are taken in the same location.

We use (15)–(18) in an iterative Jacobian inverse scheme shown in Fig. 6. The unit field maps (B_c, B_w) and their spatial derivatives are represented using rational functions of the form

$$B_\star(z) = \frac{A_\star}{z^3} + \frac{B_\star}{z^2} + \frac{C_\star}{z} + D_\star, \star = \{c, w\} \tag{19}$$

with coefficients ($A_\star, \ldots, D_\star \in \mathbb{R}$) fit to field measurements at a set of discrete locations along z.

We estimate η using an MLX90393 three-axis Hall effect sensor (Melexis NV, Ieper, Belgium) located at a point ($\mathbf{p}_s$) (Fig. 7). First, we use the sensor to create unit field maps ($\mathbf{B}_w(\mathbf{p}_s)$) and ($\mathbf{B}_c(\mathbf{p}_s)$) for windings and core at $\mathbf{p}_s$, analogously to ((13)). These field maps are subsequently used during the on-line estimation phase, alongside the real-time field measurement ($\mathbf{B}(\mathbf{p}_s)$). In that phase, η is calculated as follows:

$$\eta = \frac{\|\mathbf{B}(\mathbf{p}_s)\| - I\,\|\mathbf{B}_w(\mathbf{p}_s)\|}{I\,\|\mathbf{B}_c(\mathbf{p}_s)\|}, \quad \text{for } I \neq 0 \tag{20}$$

$$\eta = 1, \quad \text{for } I = 0. \tag{21}$$

Equation (21) holds, since, for $I = 0$, we can readily assume no saturation. Hence, we can use the relationship

($\|\mathbf{B}(\mathbf{p}_s)\| = I\,\|\mathbf{B}_c(\mathbf{p}_s)\| + I\,\|\mathbf{B}_w(\mathbf{p}_s)\|$) to reduce (20). In practice, we extend the range of (21) to $|I| < 0.1$ A, since, for low currents, the signal-to-noise ratio and the resolution for both the current and field sensors are too low for accurate on-line estimation. At the same time, the derivative ($d\eta/dI$) is approximated using a backwards finite-difference scheme.

The presented iterative map constitutes only the innermost cascade in closed-loop control of magnetic instruments. Realization of actual position control is beyond the scope of this paper since it requires substantial work related to modeling and tracking of the catheter. In practice, our iterative map could be implemented in a way similar to our previous approach [28]. ARMM could replace the actuator array used therein, which is also driven by an inverse-map approach. Alternatively, the Jacobian derived in (15), could be extended to account for the direction of the field/gradient and coupled with a model of the catheter dynamics, in a fashion similar to [5].

IV. Implementation and Experimental Results

The iterative map technique presented in Section III is implemented in C++14 on a personal computer running Linux Ubuntu 14.04. Ethernet communication is used to interface with the UR10 robot using dual server/client socket system. The system employs native URScript interface of the UR10 to communicate with the embedded position controller. This controller executes the motion of ARMM coil upon receiving a pose command, expressed as a position ($\mathbf{p}_C \in \mathbb{R}^3$) and angle-axis orientation $\mathbb{S}^3$) of the tool center-point (TCP) frame of reference ($\{\mathcal{T}\}$) (Fig. 2). This pose is retrieved as follows:

$$\mathbf{p}_C = \mathbf{p} - z\mathbf{Z}_C \tag{22}$$

$$\boldsymbol{\theta}_C = \operatorname{acos}(\widehat{\mathbf{z}} \cdot \mathbf{Z}_C)\, N(\widehat{\mathbf{z}} \times \mathbf{Z}_C) \tag{23}$$

where $\widehat{\mathbf{z}} = \begin{bmatrix}0 & 0 & 1\end{bmatrix}^T$ and $N(\boldsymbol{\alpha}) = (1/\|\boldsymbol{\alpha}\|)\boldsymbol{\alpha}\ \forall\ \boldsymbol{\alpha} \in \mathbb{R}^3$. The current in the coil is controlled directly using XEL-230-40 (Copley Controls, Boston, MA, USA) amplifier connected via EtherCAT (Fig. 2).

A. Performance and Limitations of ARMM

Several factors affect the effective workspace of the system, in terms of its capabilities of generating desired magnetic torques and forces. Our actuation method assumes that for every $\mathbf{p}$ within the effective workspace of the ARMM, the coil is capable of moving within a distance (z) along any $\mathbf{Z_c}$. To make this assumption realistic, we impose bounds ($z \in [z_{\min}, z_{\max}]$ minimum bound $z_{\min}$ is set at 50 mm such that the position of the coil is always at a safe distance, safe distance, since $\mathbf{p}$ is likely to be inside the body of a patient. The maximum bound $z_{\max}$ is selected arbitrarily at 300 mm. Furthermore, the realization of the ARMM system imposes bounds on the maximum value of the current ($|I| < 20$ A), due to the limitations of XEL-230-40.

Knowing these limits, the size of the effective workspace can be coarsely approximated. We define it as the collection of points for which the ARMM system can position its coil between ($z_{\min}$) and ($z_{\max}$) in any direction. The workspace, in which the UR10 can position its TCP in any direction, is a sphere of 1300 mm. The face of the coil is at the distance of 217 mm from the TCP. Assuming $z_{\max}$ of 300 mm, the effective workspace of the ARMM system can be approximated with a sphere with a radius of 783 mm).

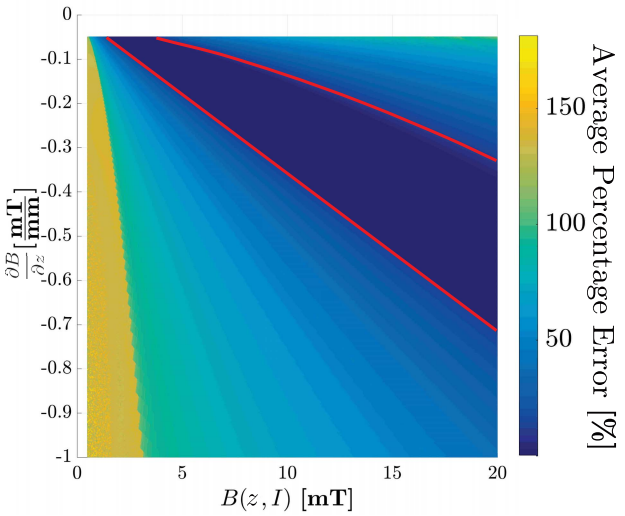

Fig. 8. Results of the simulation testing the accuracy of the iterative field map (presented in Section III) for different magnetic field/gradient setpoints ($\mathbf{b} \in \mathbb{R}^2$). The map is solved total of 10^6 different combination of $\mathbf{b}$ of the magnetic field ($B(z, I) \in \mathbb{R}$) and gradient ($\partial B/\partial z$). The solution obtained for each $\mathbf{b}$ is fed to the $\mathbf{b}$ is fed to the forward model (13), (14) to calculate the actual field and gradient it produces. The percentage error between the desired and actual $\mathbf{b}$ is calculated. The results show that imposing the bounds on the set of possible $\mathbf{q}_m$ does not result in a significant change to the $\subset \mathbf{q}_m$), which can be generated by ARMM system with errors below 10% (marked by red lines). We expect that this is due to the effect of using a damped pseudo-inverse. However, its detailed proof of lies beyond the scope of this paper.

Nevertheless, these considerations are driven by a set of simplified assumptions. The actual effective workspace of the ARMM system depends on more factors, such as the presence of obstacles or the limitations of the kinematics of UR10. In order to define a procedure-specific workspace of the device, extensive kinematic analysis needs to be performed. Furthermore, by selecting a robotic arm with a larger reach, the workspace can be easily scaled up to the desired dimensions. We believe that this feature of the mobile coil systems will, in the future, motivate their extensive use in procedures requiring magnetic actuation.

The bounds relating to limitations of the ARMM system are imposed on $\mathbf{q}_m$ upon every iteration of the map. This guarantees that, for every desired $\mathbf{b}$, the iterative map provides configuration ($\mathbf{q}_m$), which falls within the limits of the device, allowing for safe operation of ARMM. Nevertheless, by imposing these bounds, we expect its accuracy to be guaranteed only if $\mathbf{b}$ falls within a certain range of values. To quantify that range, we develop a simulation using a computational model of ARMM coil, with η being approximated using offline measurements. The results (Fig. 8) confirm our expectations, thus the accuracy of the device must be taken into account when employing the ARMM system for the steering of flexible surgical instruments.

Furthermore, Fig. 8 shows that the ARMM system can generate fields of at least 20 mT and gradients of more than 0.6 mT/mm, similar to the ones used in previous studies

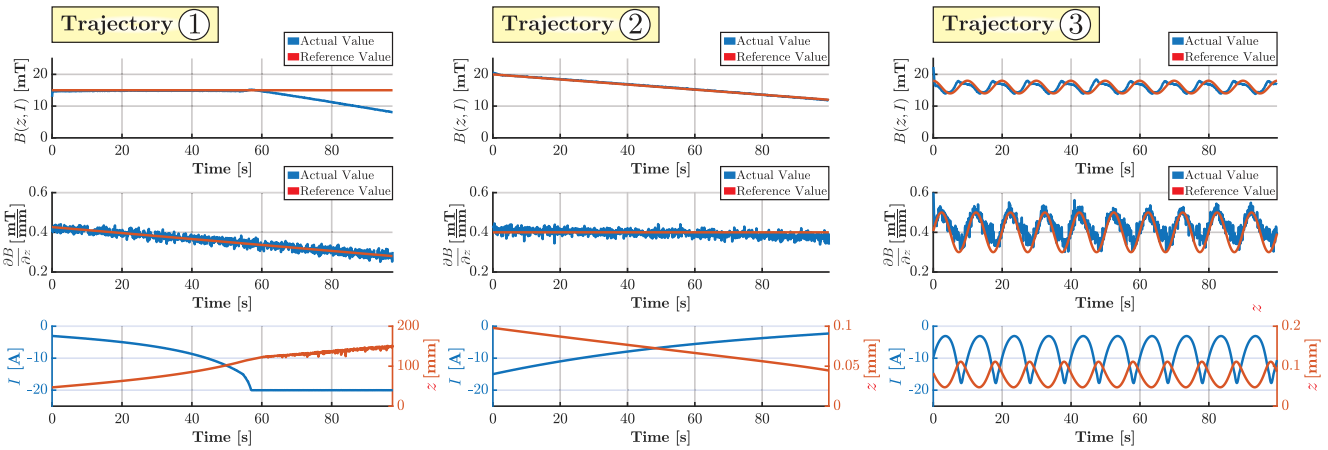

Fig. 9. Results of the experiment presented in Fig. 7. The iterative map is used to generate magnetic field/gradients following three reference trajectories. Trajectory (1) demonstrates the generation of variable gradient $\left(\frac{\partial B}{\partial z} \in \mathbb{R}\right)$ under constant magnetic field value ($B(z, I) \in \mathbb{R}$). Its final part (Time > 58 [s]) shows the effect of bounds of current (I) on the accuracy of the solution. Trajectory (2) involves a converse situation with variable field and constant current. In trajectory (3) sinusoidal functions were used to generate variation in both reference values. Disregarding the part of trajectory (1), which demonstrates the current bound, the average error across all trajectories is 2.34% for the magnetic field and 7.20% for the magnetic field gradient.

on magnetic catheters [6], [22], [24], [29]. These values by no means mark the upper limit of the system, as at a very close distances ($z < 50$ mm), the maximum field generated by the ARMM exceeds 80 mT. Thus, if collision avoidance algorithms are employed to safely keep the coil close to the skin of the patient at all times, actuation conditions comparable with commercial systems can be achieved [4], [5].

B. Experimental Validation

We validate the implementation of the iterative map experimentally (Fig. 7). We employ the ARMM system to generate a series of prescribed field/gradient trajectories for a given location ($\mathbf{p}$). The magnetic field generated by the system is measured using a Senis 3MH3A-500MT (Senis AG, Baar, Switzerland) Teslameter, while the gradient is measured indirectly by registering the force ($\mathbf{F}_\mu$) acting on a permanent magnet with known magnetic dipole moment ($\boldsymbol{\mu}$). The magnet is attached to a K3D40 force sensor (Meβsysteme AG, Henningsdorf, Germany). The force measurements are processed using (3) to obtain the final value of the magnetic gradient.

Fig. 9 shows the results from three representative trajectories. The data show good correspondence between the reference and actual values of the field and gradient, except for a region in trajectory 1, where the actual field diverges from the reference due to the solution exceeding the bound of the current (-20 A, visible on the bottom graph). This trajectory has been selected purposefully, in order to demonstrate the performance of the map in such situations. Remarkably, the generated gradient still corresponds well to the prescribed value (average error 5.57%).

Excluding the out-of-bounds region from the analysis, the average percentage error across all trajectories is 2.34% for the magnetic field and 7.2% for the magnetic field gradient. There is no significant difference between the errors in the linear ($|I| < 15$ A) and non-linear ($|I| > 15$ A) regions of coil operation. Thus, the generation of prescribed magnetic field and gradients with independently controlled magnitudes can be achieved using the iterative map to drive the ARMM system.

V. Conclusion

In this paper, the problem of achieving magnetic actuation of flexible surgical instruments (such as endovascular catheters) in large workspaces is addressed by the development of the ARMM system. By employing a mobile coil approach, the ARMM system provides magnetic actuation in a large spherical workspace. The maximum radius of that workspace (1300 mm) allows for steering magnetically actuated catheters in every point of the human body without the need of repositioning the patient. Moreover, the ARMM system employs a UR5 robotic arm that is used as an assistive device holding an ultrasound probe intended to be used as a primary medical imaging modality. The electromagnetic coil of the ARMM system employs a Vacoflux 50 ferrous core and is designed using an optimization procedure to maximize the magnetic field in the target region under payload and heat dissipation constraints. The cost function used in our procedure optimizes the geometry of the coil for the purpose of our novel magnetic actuation strategy. This strategy involves using the robotic arm to follow the position of the device in real-time, which simplifies the magnetic field models and the resulting actuation.

The results of coil characterization indicate that the optimization procedure is effective in generating coil geometries resulting in large magnetic fields, suitable for our actuation strategy. In fact, the predictions of the FE model used in the optimization routine underestimate the field generated by the real device due to the lack of accurate material model for a Vacoflux ferrous core. Since the Vacoflux core of the coil used in the ARMM system exhibits saturation within the operational range, the resulting relationship between the coil current and the magnetic field becomes non-linear. This phenomenon makes precise magnetic actuation a challenging task. We address this issue by developing a novel iterative map technique. This technique makes use of the overactuation of the ARMM system, allowing to generate magnetic fields and gradients with independently prescribed magnitudes. Furthermore, it uses a Hall effect sensor to account for the

saturation of the Vacoflux core. The technique is validated, showing an average error of 2.34% for magnetic field and 7.20% for the magnetic gradient.

In our future work, we plan to demonstrate the clinical feasibility of the ARMM system in steering magnetically actuated catheters. We will develop advanced control strategies to magnetically navigate catheters and other flexible surgical instruments in clinically relevant tasks under the guidance of medical imaging modalities. Furthermore, we will design path planning algorithms for the mobile coil to improve safety for clinicians and patients during the procedures performed by the ARMM system. Since procedure-specific considerations have a decisive impact on the required actuation, we will develop a tool for detailed kinematic analysis of the device and its limitations (e.g., singularities) during a particular procedure. Finally, we will expand the capabilities of the ARMM system by studying advanced strategies for magnetic actuation, which involve more than one optimally designed mobile coil, and account for phenomena neglected in this work, such as coil hysteresis or crosstalk between multiple cores.

ACKNOWLEDGMENT

This work was supported in part by the European Research Council (ERC) through the European Unions Horizon 2020 Research and Innovation Program under Grant #638428 (Project ROBOTAR) and in part by the Netherlands Organization for Scientific Research (NWO) through the Innovational Research Incentives Scheme under Grant VIDI #14855 (Project SAMURAI).

REFERENCES

[1] H. Q. Ontario, "Coil embolization for intracranial aneurysms: An evidence-based analysis," *Ontario Health Technol. Assessment Ser.*, vol. 6, no. 1, pp. 1–114, 2006.

[2] N. Gudino, J. A. Heilman, J. J. Derakhshan, J. L. Sunshine, J. L. Duerk, and M. A. Griswold, "Control of intravascular catheters using an array of active steering coils," *Med. Phys.*, vol. 38, no. 7, pp. 4215–4224, 2011.

[3] A. Ali, D. H. Plettenburg, and P. Breedveld, "Steerable catheters in cardiology: Classifying steerability and assessing future challenges," *IEEE Trans. Biomed. Eng.*, vol. 63, no. 4, pp. 679–693, Apr. 2016.

[4] C. M. Heunis, J. Sikorski, and S. Misra, "Magnetic actuation of flexible surgical instruments for endovascular interventions," *IEEE Robot. Autom. Mag.*, vol. 25, no. 3, pp. 71–82, Sep. 2018.

[5] J. Edelmann, A. J. Petruska, and B. J. Nelson, "Magnetic control of continuum devices," *Int. J. Robot. Res.*, vol. 36, no. 1, pp. 68–85, 2017.

[6] J. Sikorski, I. R. Dawson, A. Denasi, E. E. G. Hekman, and S. Misra, "Introducing BigMag—A novel system for 3D magnetic actuation of flexible surgical manipulators," in *Proc. IEEE Int. Conf. Robot. Automat. (ICRA)*, Singapore, May/Jun. 2017, pp. 3594–3599.

[7] M. P. Kummer, J. J. Abbott, B. E. Kratochvil, R. Borer, A. Sengul, and B. J. Nelson, "OctoMag: An electromagnetic system for 5-DOF wireless micromanipulation," *IEEE Trans. Robot.*, vol. 26, no. 6, pp. 1006–1017, Dec. 2010.

[8] I. Tunay, "Position control of catheters using magnetic fields," in *Proc. IEEE Int. Conf. Mechatron. (ICM)*, Jun. 2004, pp. 392–397.

[9] S. E. Wright, A. W. Mahoney, K. M. Popek, and J. J. Abbott, "The spherical-actuator-magnet manipulator: A permanent-magnet robotic end-effector," *IEEE Trans. Robot.*, vol. 33, no. 5, pp. 1013–1024, Oct. 2017.

[10] I. S. M. Khalil, B. E. Wissa, B. G. Salama, and S. Stramigioli, "Wireless motion control of paramagnetic microparticles using a magnetic-based robotic system with an open-configuration," in *Proc. IEEE Int. Conf. Manipulation, Manuf. Meas. Nanosc. (3M-NANO)*, Oct. 2015, pp. 190–196.

[11] L. B. Kratchman, T. L. Bruns, J. J. Abbott, and R. J. Webster, III, "Guiding elastic rods with a robot-manipulated magnet for medical applications," *IEEE Trans. Robot.*, vol. 33, no. 1, pp. 227–233, Feb. 2016.

[12] P. R. Slawinski, A. Z. Taddese, K. B. Musto, K. L. Obstein, and P. Valdastri, "Autonomous retroflexion of a magnetic flexible endoscope," *IEEE Robot. Autom. Lett.*, vol. 2, no. 3, pp. 1352–1359, Jul. 2017.

[13] B. Veron, A. Hubert, J. Abadie, N. Andreff, and P. Renaud, "Advocacy for multi mobile coil magnetic manipulation in active digestive endoscopy," in *Proc. IEEE/RSJ Int. Conf. Intell. Robots Syst. (IROS)*, 2012, p. 2.

[14] B. Véron, J. Abadie, A. Hubert, and N. Andreff, "Magnetic manipulation with several mobile coils towards gastrointestinal capsular endoscopy," in *New Trends in Mechanism and Machine Science* (Mechanisms and Machine Science). New York, NY, USA: Springer, 2013, pp. 681–689.

[15] G. Lucarini, G. Ciuti, M. Mura, R. Rizzo, and A. Menciassi, "A new concept for magnetic capsule colonoscopy based on an electromagnetic system," *Int. J. Adv. Robot. Syst.*, vol. 12, no. 3, p. 25, 2015.

[16] G. Lucarini, M. Mura, G. Ciuti, R. Rizzo, and A. Menciassi, "Electromagnetic control system for capsule navigation: Novel concept for magnetic capsule maneuvering and preliminary study," *J. Med. Biol. Eng.*, vol. 35, no. 4, pp. 428–436, 2015.

[17] J. J. Abbott and B. Osting, "Optimization of coreless electromagnets to maximize field generation for magnetic manipulation systems," *IEEE Magn. Lett.*, vol. 8, 2017, Art. no. 1300104.

[18] D. J. Griffiths and C. Inglefield, *Introduction to Electrodynamics*, 3rd ed. Upper Saddle River, NJ, USA: Prentice-Hall, 2005.

[19] C. Chautems and B. J. Nelson, "The tethered magnet: Force and 5-DOF pose control for cardiac ablation," in *Proc. IEEE Int. Conf. Robot. Autom. (ICRA)*, Singapore, May/Jun. 2017, pp. 4837–4842.

[20] S. Muntwyler, B. Kratochvil, B. Nelson, D. Frutiger, D. Bell, and J. Baumann, "Magnetic navigation system with soft magnetic core electromagnets for operation in the non-linear regime," U.S. Patent 9 681 859 B2, Jun. 20, 2017.

[21] F. Beyeler, S. Muntwyler, Z. Nagy, C. Graetzel, M. Moser, and B. J. Nelson, "Design and calibration of a MEMS sensor for measuring the force and torque acting on a magnetic microrobot," *J. Micromech. Microeng.*, vol. 18, no. 2, 2007, Art. no. 025004.

[22] F. Ullrich, S. Schuerle, R. Pieters, A. Dishy, S. Michels, and B. J. Nelson, "Automated capsulorhexis based on a hybrid magnetic-mechanical actuation system," in *Proc. IEEE Int. Conf. Robot. Automat. (ICRA)*, Hong Kong, China, May/Jun. 2014, pp. 4387–4392.

[23] C. Chautems, A. Tonazzini, D. Floreano, and B. J. Nelson, "A variable stiffness catheter controlled with an external magnetic field," in *Proc. IEEE/RSJ Int. Conf. Intell. Robots Syst. (IROS)*, Sep. 2017, pp. 181–186.

[24] K. J. Boskma, S. Scheggi, and S. Misra, "Closed-loop control of a magnetically-actuated catheter using two-dimensional ultrasound images," in *Proc. IEEE 6th Int. Conf. Biomed. Robot. Biomechatron. (BioRob)*, Singapore, Jun. 2016, pp. 61–66.

[25] R. C. Dorf, *The Electrical Engineering Handbook*. Boca Raton, FL, USA: CRC Press, 1997.

[26] V. N. T. Le, N. H. Nguyen, K. Alameh, R. Weerasooriya, and P. Pratten, "Accurate modeling and positioning of a magnetically controlled catheter tip," *Med. Phys.*, vol. 43, no. 2, pp. 650–663, 2016.

[27] S. Chiaverini, B. Siciliano, and O. Egeland, "Review of the damped least-squares inverse kinematics with experiments on an industrial robot manipulator," *IEEE Trans. Control Syst. Technol.*, vol. 2, no. 2, pp. 123–134, Jun. 1994.

[28] J. Sikorski, A. Denasi, G. Bucchi, S. Scheggi, and S. Misra, "Vision-based 3-D control of magnetically actuated catheter using BigMag—An array of mobile electromagnetic coils," *IEEE/ASME Trans. Mechatronics*, vol. 24, no. 2, pp. 505–516, Apr. 2019.

[29] S. L. Charreyron, B. Zeydan, and B. J. Nelson, "Shared control of a magnetic microcatheter for vitreoretinal targeted drug delivery," in *Proc. IEEE Int. Conf. Robot. Automat. (ICRA)*, May/Jun. 2017, pp. 4843–4848.